3D Echo Planar Time-resolved Imaging (3D-EPTI) for ultrafast multi-parametric quantitative MRI

Fuyixue Wang[a,b,c,1,*], **Zijing Dong**[a,d,1], **Timothy G. Reese**[a,c], **Bruce Rosen**[a,b,c], **Lawrence L. Wald**[a,b,c], **Kawin Setsompop**[e,f]

[a]Athinoula A. Martinos Center for Biomedical Imaging, Massachusetts General Hospital, Charlestown, Massachusetts, USA

[b]Harvard-MIT Health Sciences and Technology, MIT, Cambridge, Massachusetts, USA

[c]Department of Radiology, Harvard Medical School, Boston, Massachusetts, USA

[d]Electrical Engineering and Computer Science, MIT, Cambridge, Massachusetts, USA

[e]Department of Radiology, Stanford University, Stanford, USA

[f]Department of Electrical Engineering, Stanford University, Stanford, USA

Abstract

Multi-parametric quantitative MRI has shown great potential to improve the sensitivity and specificity of clinical diagnosis and to enhance our understanding of complex brain processes, but suffers from long scan time especially at high spatial resolution. To address this longstanding challenge, we introduce a novel approach termed 3D Echo Planar Time-resolved Imaging (3D-EPTI), which significantly increases the acceleration capacity of MRI sampling, and provides high acquisition efficiency for multi-parametric MRI. This is achieved by exploiting the spatiotemporal correlation of MRI data at multiple timescales through new encoding strategies within and between efficient continuous readouts. Specifically, an optimized spatiotemporal CAIPI encoding within the readouts combined with a radial-block sampling strategy across the readouts enables an acceleration rate of 800 fold in the *k-t* space. A subspace reconstruction was employed to resolve thousands of high-quality multi-contrast images. We have demonstrated the ability of 3D-EPTI to provide robust and repeatable whole-brain simultaneous T_1, T_2, T_2*, PD and B_1^+ mapping at high isotropic resolution within minutes (e.g., 1-mm isotropic resolution in 3 minutes), and to enable submillimeter multi-parametric imaging to study detailed brain structures.

*Corresponding author at: Athinoula A. Martinos Center for Biomedical Imaging, Charlestown, MA, 02129, United States. fwang18@mgh.harvard.edu (F. Wang).
[1]These authors contribute equally to the manuscript.

Keywords

Quantitative MRI; EPTI; Fast imaging; Multi-parametric; High resolution; Relaxometry

1. Introduction

Multiparametric MRI provides quantitative measurements that are sensitive to a variety of tissue properties of the human brain. Its quantitative nature leads to less reliance on system conditions and human interpretation compared to standard qualitative images, and makes it possible to measure tissue properties among populations or along time, therefore providing great potentials to improve clinical diagnosis (Bernasconi et al., 1999; Falangola et al., 2007; Lescher et al., 2015; Ma et al., 2018b; Müller et al., 2017; Ramani et al., 2006; Reitz et al., 2017; Tardif et al., 2011; Tofts, 2005; West et al., 2014) or to enhance our understanding of complex brain processes such as brain development or aging (Bozzali et al., 2016; Filo et al., 2019; Sled and Nossin-Manor, 2013).

A major limitation of quantitative multiparametric MRI is its long acquisition time. This is due to the need to acquire a series of multi-contrast images in order to perform model fittings for quantitative parameter estimation, as well as the need to repeat such process for each parameter in multiparametric imaging. Acceleration of the acquisition has been made possible by using parallel imaging (Griswold et al., 2002; Pruessmann et al., 1999; Sodickson and Manning, 1997) or by enforcing prior knowledge of image properties through compressed-sensing theory (Lustig et al., 2007), both of which can help recover undersampled k-space. Together with new pulse sequence design, many fast quantification methods have been developed to obtain multiple parameters simultaneously (e.g., T_1, T_2, T_2*) (Caan et al., 2019; Deoni et al., 2003; Fujita et al., 2019; Krauss et al., 2015; Metere et al., 2017; Warntjes et al., 2007; Warntjes et al., 2008). However, the ability to accelerate the acquisition is still limited and obtaining high-resolution multi-parametric MRI in clinical acceptable time remains a challenge.

Recently, an emerging area of research has been in the use of spatiotemporal correlation to achieve high acceleration for quantitative MRI. For example, MR fingerprinting (Boyacioglu et al., 2021; Cloos et al., 2016; Hong et al., 2019; Jiang et al., 2015; Liao et al., 2017; Ma et al., 2013, 2018a, b; Wyatt et al., 2018) and MR multitasking (Christodoulou et al., 2018; Ma et al., 2020, Ma et al., 2021) have utilized spatiotemporal correlation between readouts after different RF excitations to accelerate multi-parametric imaging, which have shown promising results especially when used in conjunction with the low-rank subspace model (Christodoulou et al., 2018; Lam and Liang, 2014; Liang, 2007; Tamir et al., 2017; Zhao et al., 2018). Another approach, Echo Planar Time-resolved Imaging (EPTI) (Dong et al., 2021a; Dong et al., 2020; Wang et al., 2019a; Wang et al., 2019b; Wang et al., 2021), has been developed recently to provide dense data sampling and exploit the spatiotemporal correlation within a continuous EPI-like readout. Within the readout, data are densely sampled at a short timescale (submillisecond), so only minimal phase accumulation and signal decay will occur, resulting in high temporal correlation to reconstruct the highly-accelerated data. In addition, it takes advantage of the spatial information from multi-

channel coils by employing a novel spatiotemporal encoding strategy within the readout for further acceleration. The continuous EPTI readout enables high sampling efficiency with minimal dead time, while the time-resolving approach across the readout eliminates the undesirable image distortion and blurring common in the conventional EPI (Mansfield, 1977), providing a series of high quality multi-contrast images sampled at small time interval that can continuously track the signal evolution. We have demonstrated efficient whole brain T_2 and T_2* mapping using a GE-SE EPTI sequence at 1.1-mm in-plane resolution within 28 s in our previous work (Wang et al., 2019a).

Here, in pursuit of a significant further increase in acceleration capability, 3D-EPTI has been developed. 3D-EPTI extends the spatiotemporal EPTI encoding from 2D (k_y-t) to 3D (k_y-k_z-t), and develops a new data sampling strategy with a combined controlled- and incoherent-aliasing scheme. Data correlations at multiple timescales are exploited, both within and between the continuous readouts. Within readouts, a spatiotemporal encoding is designed with complementary sampling in a controlled-aliasing (Breuer et al., 2005; Breuer et al., 2006; Dong et al., 2019) (CAIPI) pattern in the k_y-k_z-t domain, which uses the coil sensitivity information along both the partition and phase encoding directions along with the temporal correlation across echoes, and offers a high acceleration capacity (e.g., $80 \times$ in k-t). Between readouts, a novel radial-block encoding is developed to exploit data correlation in a longer timescale based on the compressed sensing theory (Lustig et al., 2007). The radial-block sampling creates incoherent aliasing along time that can be well excluded from the coherent signal evolutions, therefore provides another $10 \times$ acceleration in k-t space. The integration of the continuous readout, the spatiotemporal CAIPI and the radial-block encoding provides datasets with high correlation, which allows for ~$800 \times$ acceleration in the spatiotemporal domain and enables reconstruction of thousands of multi-contrast 3D images by combining with the low-rank subspace reconstruction approach (Dong et al., 2020; Guo et al., 2021; He et al., 2016; Lam and Liang, 2014; Liang, 2007; Meng et al., 2021; Tamir et al., 2017; Zhao et al., 2015). While this acquisition scheme can be applied or adapted to any sequence or other types of readouts to track the signal evolution and to measure a variety of quantitative parameters, this work employs specific sequence to simultaneously obtain MR relaxation time constants T_1, T_2, T_2* as well as RF field inhomogeneity (B_1+) and proton density (PD). We demonstrated the ability of 3D-EPTI to acquire high-quality whole-brain multi-parametric maps at isotropic 1.5-mm in 1 minute or at isotropic 1-mm in 3 minutes with high repeatability and reliability. An isotropic 0.7-mm 3D-EPTI protocol was also developed to enable, for the first time, the examination of simultaneously acquired T_1, T_2, and T_2* in less than 10 minutes to help better investigate the intra-cortical architecture.

2.   Material and methods

2.1.   3D-EPTI overview

3D-EPTI acquires highly-accelerated k-t data using continuous readouts to track signal evolutions with minimal deadtime and high readout efficiency. Time-varying undersampling patterns are employed to exploit the spatiotemporal correlation within and among readouts for robust reconstruction at high acceleration. In the time domain, the full signal evolutions

are represented by a small number of low-rank subspace bases in the reconstruction process to reduce the number of unknowns. In the spatial domain, the time-varying complementary sampling further improves the reconstruction based on principles of parallel imaging (Griswold et al., 2002; Pruessmann et al., 1999; Sodickson and Manning, 1997) and compressed sensing (Lustig et al., 2007). Parallel imaging helps the recovery of undersampling by taking advantage of the CAIPI-like k-t controlled aliasing patterns. Compressed sensing (in the form of low-rank regularization on the basis coefficient maps) further reduces aliasing by exploiting the incoherence of the aliasing patterns along both the spatial and temporal dimensions. After reconstruction, the signal evolution at each voxel is obtained, expressed as a linear combination of the temporal subspace bases, which will then be used to match the simulated signal evolutions (dictionary) to estimate the quantitative parameters.

2.2. 3D-EPTI acquisition

Fig. 1 illustrates the 3D-EPTI acquisition. An inversion-recovery gradient echo (IR-GE) and a variable-flip-angle gradient-and-spin-echo (Feinberg and Oshio, 1991; Oshio and Feinberg, 1991) (VFA-GRASE) sequence (Fig. 1a) were employed to provide signal evolutions that are sensitive to T_1, T_2, and T_2^* relaxations (Fig. 1b). After each RF excitation, a 3D-EPTI readout is acquired, which continuously captures the temporal signal evolution with efficient bipolar gradient. To resolve images within the readout with high acceleration, a spatiotemporal CAIPI encoding is employed in a 4D spatiotemporal (k_x-k_y-k_z-t) domain (Fig. 1d, the readout dimension k_x is fully-sampled and therefore omitted in the illustration). At each time point within the readout, a particular phase and partition position (k_y-k_z) is acquired that is interleaved to its neighboring time points in a 'controlled-aliasing' pattern. Across a slightly longer timescale, two complementary patterns are interleaved across echoes (orange and green points in Fig. 1d, different 'echo sections', each contains multiple echoes) to provide more independent k-space sampling locations, which has been shown to further improve the reconstruction performance at high acceleration rates (Dong et al., 2020). Each 3D-EPTI readout covers a relatively small block in k_y-k_z-t space to ensure that the neighboring k_y-k_z samplings are close in time. The CAIPI pattern, the complementary sampling across echoes, and the proximity in time together result in high spatiotemporal correlation and allow for effective use of the available coil sensitivity information. Therefore, the highly-undersampled data (e.g., undersampling rate = 80 × in k-t space) at each time point can be well reconstructed, resolving a series of images across the readout at a submillisecond time interval (Fig. 1d, left).

In each repetition time (TR), multiple k-t blocks can be acquired across multiple readouts after different excitations (Fig. 1c, blocks in the same color are acquired in the same TR). Here, TR refers to the overall repetition time of IR-GE or VFA-GRASE, and therefore includes multiple readouts (e.g., in IR-GE, it includes the time for an inversion pulse and the following multiple small-flip-angle GE excitations). To quickly encode the 4D k-t space using a small number of TRs, a golden-angle radial-block Cartesian sampling is employed across different readouts. Specifically, the blocks acquired after the same excitation in different TRs form a diagonal radial blade in the k_y-k_z space, with different blade angulations across different readouts. This was developed to create a favorable

spatiotemporal incoherent aliasing across the readouts that is well suited for constrained reconstruction, which permits a further ~10 × acceleration through acquiring only a few blades for each readout instead of the full k_y-k_z sampling.

2.3. Image reconstruction

The acquired highly undersampled data will then be reconstructed by a low-rank subspace reconstruction (Dong et al., 2020; Guo et al., 2021; He et al., 2016; Lam and Liang, 2014; Liang, 2007; Meng et al., 2021; Tamir et al., 2017; Zhao et al., 2015) to time-resolve thousands of multi-contrast images (Fig. 2). The low-rank subspace method was used to improve the conditioning of the EPTI reconstruction by using the low-rank prior information of the signal evolution, as demonstrated in our previous work (Dong et al., 2020).

At first, a large number of temporal signal evolutions are simulated using the Extended Phase Graphs (EPG) approach (Weigel, 2015), each contains N_t (e.g., 1350 for the 1-mm protocol) time points. A wide range of quantitative parameters were used to exhaust all possibilities of the interest (e.g., T_1: 400 ms to 5000 ms, T_2: 10 ms to 500 ms, T_2^*: 10 ms to 500 ms, B_1^+ factor: 0.75 to 1.25). Second, N_b subspace basis vectors $\phi \in \mathbb{C}^{N_t \times N_b}$ are extracted from these simulated signals by using principal component analysis (PCA). In this study, 12 bases were selected that can approximate the simulated signals with an error smaller than 0.2%. Then, the full time series of N_v spatial voxels can be represented by ϕc, where $c \in \mathbb{C}^{N_b \times N_v}$ represents the coefficient maps of the subspace bases that can be estimated by solving:

$$\min_c \| U\,F\,S\,P\phi c - y \|_2^2 + \lambda R(c) \tag{1}$$

where $P \in \mathbb{C}^{N_v \times N_t}$ contains the phase evolutions across the time-series images including the background and B_0 inhomogeneity-induced phases, $S \in \mathbb{C}^{N_v \times N_c}$ denotes the coil sensitivity of a N_c-channel receiver coil, F is the Fourier transform operator, U is the undersampling mask, and y represents the acquired k-space data. The phase map P and sensitivity map S can be obtained from a fast low-resolution calibration pre-scan. A locally low-rank (LLR) (Trzasko et al., 2011; Zhang et al., 2015) regularization $R(c)$ is applied on coefficient maps in the spatial domain to further improve the conditioning with a control parameter λ. A λ of 0.0003 was empirically selected based on the evaluation of RMSEs in a simulation test, where pre-acquired quantitative maps were used to generate k-t data which were then added with noise and undersampled to evaluate 3D-EPTI reconstruction errors (details in Supplementary Fig. 3). Before reconstruction, 1D linear phase difference between odd and even echoes was removed based on the phase estimation from the calibration data similar to the ghost-correction process in conventional EPI.

For 3D-EPTI, the use of temporal correlation through subspace reconstruction is the major solver of the highly-accelerated data, with a reduction factor of 112 for unknowns (e.g., 1350 images to 12 bases), and the use of spatial information from parallel imaging and low-rank constraints further improves the conditioning and helps with the acceleration.

After reconstruction, the quantitative values can be obtained by matching the signal evolution with a pre-calculated dictionary (including T_1, T_2, T_2, PD and B_1^+) generated using the EPG approach (Weigel, 2015). After dictionary matching, the estimated 3D B_1^+ maps are first fitted by a 2nd-order polynomial function in the spatial domain to remove residual noise and artifacts, with an assumption that B_1^+ fields vary smoothly in the spatial domain. Then, the quantitative parameters of each voxel are re-estimated by dictionary matching using the signal evolution simulated with the estimated B_1^+ value.

2.4. In-vivo experiments and acquisition parameters

All data were acquired on a Siemens Prisma 3T scanner with a 32-channel head coil (Siemens Healthineers, Erlangen, Germany). Informed consent was collected from all healthy volunteers before scanning, with an institutionally approved protocol.

The details of the pulse sequence used in our experiments are described here. In the IR-GE sequence, an adiabatic inversion pulse was applied, followed by 20 excitation pulses with a small flip angle (FA) of 30°. In the VFA-GRASE sequence, 10 variable-flip-angle refocusing pulses were applied after the 90° pulse with FAs of 122°, 58°, 44°, 41°, 41°, 46°, 158°, 189°, 43°, 30°. The FAs were chosen based on the results of an optimization considering both the signal amplitude and the differentiability between tissues (Cohen and Polimeni, 2018). The values were searched in empirical ranges using 'fmincon' function in MATLAB. All the excitation and refocusing RF pulses in the IR-GE and GRASE sequences were non-selective with short pulse durations (0.5 ms for excitation and 1 ms for refocusing), resulting in short starting TE and sampling interval. Readout gradient was applied along the Head-Foot (HF) direction to avoid signal wrap from the non-selective excitation. Spectrally-selective fat saturation was applied before excitation.

To evaluate the repeatability of 3D-EPTI, a scan-rescan assessment was performed on 5 healthy volunteers using a 3-minute 1-mm 3D-EPTI protocol, where the subjects were taken out of the scanner and repositioned between the two scans. The data were acquired with the following parameters: FOV = $220 \times 176 \times 210$ mm^3 (AP-z, LR-y, HF-x), matrix size = $230 \times 184 \times 210$, spatial resolution = $0.96 \times 0.96 \times 1$ mm^3, echo spacing = 0.93 ms, TR of IR-GE = 2600 ms, TR of GRASE = 800 ms, block size ($k_y \times k_z$) = 8×10 ($80 \times k$-t acceleration, see Supplementary Fig. 1a for encoding pattern). There were 20 readouts in IR-GE, each containing 48 echoes, and 10 readouts in GRASE, each containing 39 echoes. 2 radial lines were acquired for the IR-GE sequence (in a total of 45 TRs, instead of 23 $\times$ 23 = 529 TRs without radial-block acceleration), and 3 radial lines in a total of 67 TRs were acquired for the GRASE sequence (Supplementary Fig. 2 top row). More lines were acquired in GRASE to compensate for the fewer number of readouts to encode the k-t space. The total acquisition time was ~3 minutes, including 117 seconds for IR-GE, 54 seconds for GRASE, and a 12-second calibration scan. The k-t calibration scan was acquired to estimate the B_0 and coil sensitivity using a GE sequence with bipolar readouts with the following parameters: matrix size = $42 \times 32 \times 210$, number of echoes = 9, TR = 24 ms. The k-space center (8×8) was fully-sampled and the rest of k-space was undersampled along k_y and k_z by a factor of 2×2. GRAPPA (Griswold et al., 2002) was used to reconstruct the missing

data points in the calibration data. The calibration scan for all of the following acquisitions used the same matrix size along k_y and k_z with the same acceleration factor.

Two additional whole-brain protocols at different resolutions were also acquired. i) A fast 1-min 1.5-mm protocol: FOV = 218 × 173 × 230 mm^3 (AP-z, LR-y, HF-x), matrix size = 150 × 120 × 154, spatial resolution = 1.45 × 1.44 × 1.49 mm^3, echo spacing = 0.72 ms, TR of IR-GE = 1900 ms, TR of GRASE = 600 ms, block size (k_y × k_z) = 8 × 10 (80 × k-t acceleration, see Supplementary Fig. 1a for encoding pattern), each readout contained 53 echoes in IR-GE, and 39 echoes in GRASE. 3 radial lines with a reduction factor of 2 along the radial direction, equivalent to 1.5 lines, were acquired in a total of 23 TRs (instead of 15 × 15 = 225 TRs), and 2 radial lines were acquired for GRASE in 29 TRs (Supplementary Fig. 2 middle row). The total acquisition time was ~ 1 minute, including 44 s for IR-GE and 17 s for GRASE. The 1.5-mm calibration scan took 10 seconds with a TR = 20 ms. ii) A high resolution 9-min 0.7-mm protocol with acquisition parameters: FOV = 224 × 176.4 × 224 mm^3 (AP-y, LR-z, HF-x), matrix size = 328 × 246 × 322, spatial resolution = 0.68 × 0.72 × 0.70 mm^3, echo spacing = 1.2 ms, TR of IR-GE = 2600 ms, TR of GRASE = 800 ms, block size (k_y × k_z) = 8 × 6 (48 × k-t acceleration, see Supplementary Fig. 1b for encoding pattern), each readout contained 42 echoes in IR-GE, and 33 echoes in GRASE. 4 radial lines were acquired for both IR-GE and GRASE in a total of 161 TRs (instead of 41 × 41 = 1681 TRs) to provide sufficient sampling for higher spatial resolution (Supplementary Fig. 2 bottom row). The total acquisition time was ~ 9 minutes, including 7 minutes for IR-GE and 2 minutes for GRASE. The calibration scan took 12 seconds with 7 echoes and a TR of 24 ms.

To further validate 3D-EPTI's reliability, a comparison study between quantitative parameters provided by 3D-EPTI and those from lengthy standard acquisition methods was conducted both in a custom-made agar phantom and *in vivo*. For 3D-EPTI acquisition, the 1-mm 3D-EPTI protocol described above was used. The standard acquisition includes a 2D IR-SE sequence for T_1 mapping, a 2D single-echo SE sequence for T_2 mapping, and a 3D multi-echo GRE sequence for T_2* mapping. In the phantom experiment, the acquisition parameters of the 2D IR-SE sequence were: FOV = 256 × 256 mm^2, in-plane resolution = 1 × 1 mm^2, slice thickness = 3 mm, number of slices = 9, acceleration factor along k_y = 2, TR = 8000 ms, TIs = 100, 200, 400, 800, 1600, 3200 ms. The 2D single-echo SE sequence acquired 6 echo times (25, 50, 75, 100, 150, 200 ms) with a TR of 3000 ms, and used the same FOV, resolution, and acceleration as the IR-SE. The 3D multi-echo GRE sequence used for the T_2* mapping was acquired with a FOV of 186 × 176 × 224 mm^3 at 1-mm isotropic resolution. Seven echo times (5, 10, 15, 25, 35, 45, 60 ms) were acquired with an acceleration factor of 2 × 2 (k_y × k_z). The total acquisition time for the phantom scan was about 1.5 hours, including 30 minutes for IR-GE, 50 minutes for single-echo SE, and 12 minutes for 3D GRE. The same sequences were used for the in-vivo test, but at a lower resolution of 2 × 2 mm^2 in the IR-SE and single-echo SE sequences (for T_1 and T_2 measurements) to reduce the scan time and mitigate potential motion-induced artifacts (T_2* was acquired at matched resolution with 3D-EPTI). Most of the other parameters were kept the same as the phantom scan, except for: the number of slices = 19 for IR-SE and single-echo SE; TEs of single-echo SE = 25, 50, 75, 100, 140, 180 ms; a higher acceleration factor along k_y = 3 for IR-GE and single-echo SE; and FOV of 3D-GRE = 216 × 176 × 210

mm^3. Even with the lower resolution and higher acceleration, the total scan time was still about 53 minutes, including 27 minutes for single-echo SE, 14 minutes for IR-SE, and 12 minutes for GRE.

2.5. Image processing and analysis

Data reconstructions were performed in MATLAB using a Linux workstation (CPU: Intel Xeon, 3.00 GHz, 24 Cores; RAM: 512 GB; GPU: Quadro RTX 5000, 16 GB memory). The subspace reconstruction was solved by the alternating direction method of multipliers (ADMM) algorithm (Boyd et al., 2011) implemented in the Berkeley Advanced Reconstruction Toolbox (BART) (Tamir et al., 2016; Uecker et al., 2015). The whole-volume reconstruction time of the 1-mm dataset was about 3 hours on GPU.

In the test-retest experiment, the quantitative maps from the two scans (3-min 1-mm protocol) were first registered using FSL FLIRT (Jenkinson et al., 2002; Jenkinson et al., 2012; Jenkinson and Smith, 2001). Then, the averaged R_1 maps of each subject were used for Freesurfer (Desikan et al., 2006; Fischl, 2012; Fischl et al., 2002) segmentation, which resulted in 165 Region Of Interests (ROI) (listed in Supplementary Table 1) in cortical, subcortical, white matter and cerebellum regions, after removing CSF regions and ROIs smaller than 50 voxels. In the comparison experiment between 3D-EPTI and the standard acquisitions, auto-segmentation is challenging due to limited number of slices with slice gaps in the lengthy standard acquisition, so the ROI analysis was performed in 14 manually-selected anatomical ROIs (details listed in Supplementary Table 2) that were contained within the slice coverage of the standard 2D acquisitions. Two-sided t-tests and Pearson's correlation coefficients were used in the analysis.

Surface-based cortical reconstruction was performed using Freesurfer (Desikan et al., 2006; Fischl, 2012; Fischl et al., 2002) on the R_1 maps separately for each subject and for each scan (9-min 0.7-mm protocol). 9 equi-volume (Waehnert et al., 2014; Waehnert et al., 2016) cortical layers were reconstructed, and applied to all quantitative maps to investigate their distribution across different cortical depths. These maps were sampled onto the average subject space with a 2-mm Gaussian surface smoothing for final analysis.

Although quantitative imaging provides a more direct measurement of tissue properties, contrast-weighted images are still used in current clinical routine. Here we evaluated image synthesis using 3D-EPTI to provide multiple image contrasts without additional scans. Synthetic images were synthesized from the quantitative maps based on the signal equations of the specific sequences. In addition, parameters that determine the contrast (e.g., TI and TE of the IR-SE sequence) were adjusted in a wide range to generate a spectrum of contrast differences between tissues. The parameters that generated the maximal difference were selected to obtain images with improved contrast and visualization.

3. Results

3.1. Simultaneous T_1, T_2, and T_2* mapping in 3-minutes at 1-mm isotropic resolution

Fig. 3 demonstrates an example dataset acquired by 3D-EPTI at 1-mm isotropic resolution with whole brain coverage in 3 minutes, resulting in a total of 1350 multi-contrast images

resolved at a time interval of 0.93 ms (an echo-spacing). Representative images with different T_1, T_2, T_2* contrasts reconstructed from the highly undersampled dataset are shown in Fig. 3a. The resultant quantitative parameter T_1, T_2, T_2*, PD maps show high image SNR and resolution, without image distortions and noticeable aliasing artifacts (Fig. 3b). In addition to these quantitative parameters, the B_1^+ field was also estimated from the same dataset to reduce potential bias for relaxometry. These multi-parametric maps acquired in a single scan are perfectly aligned without the need for co-registration. A more comprehensive view of these images in three orthogonal planes across all slices for the three quantitative parameter maps are provided in the Supplementary Movie 1–3 (de-faced images). The accuracy of the quantitative estimates, including T_1, T_2, T_2*, PD and B_1^+, was also tested through a simulation experiment with gold standard reference parameter maps (pre-acquired quantitative maps, which were used to generate undersampled *k-t* data to evaluate the reconstruction and quantitative estimation). As shown in Supplementary Fig. 3, low errors are observed for all parameters in gray and white matters, while CSF shows a higher level of errors.

3.2. Characterization of the repeatability and reliability for T_1, T_2, and T_2* mapping

To evaluate the repeatability of 3D-EPTI, the scan-rescan assessment performed on 5 healthy volunteers using the 3-minute 1-mm protocol is shown in Fig. 4. An example of the 165 auto-segmented Freesurfer ROIs used in the study is demonstrated in Fig. 4a. High correlations were measured between the two scans for all three parameters as shown in Fig. 4b. Specifically, the measurements from the first and the second scans are highly correlated with a positive Pearson's correlation coefficient (PCC) of 0.996 (P < 0.0001) for T_1, 0.974 (P < 0.0001) for T_2 and 0.938 (P < 0.0001) for T_2* (previously reported in-vivo MRF test-retest repeatability in a voxel-wise evaluation (Buonincontri et al., 2019): PCC = ~0.96 for T_1 and PCC = ~0.94 for T_2 in white matter). The scan-rescan difference maps (Fig. 4d) show a low level of differences and a relative homogeneous distribution in the gray and white matter areas of interest, while larger differences are observed in CSF and deep brain regions.

The intra-subject variability between test-retest scans and inter-subject variability among the five volunteers were also evaluated and compared using coefficient of variation (COV). Fig. 4c shows the distribution of the intra-subject and inter-subject COVs across all ROIs in box plots with whiskers from minimum to maximum data points. The intra-subject variability was measured with a median COV at 0.93%, 1.88% and 2.27% for T_1, T_2 and T_2* respectively (previously reported MRF average intra-subject COV for T_1 and T_2 is 3.1% (Ma et al., 2018b)). The inter-subject COVs were measured with median COVs at 2.39%, 4.75%, 5.09% for T_1, T_2 and T_2* (previously reported MRF average inter-subject COV for T_1 and T_2 is 4.3% (Ma et al., 2018b)), which are higher than the intra-subject measurements as expected. The overall low level of COVs demonstrates the high level of repeatability of the 3D-EPTI quantifications, while the expected differences between intra- and inter-subject suggest the potential ability of 3D-EPTI in capturing individual differences. Among the three parameters, T_2* shows the largest variability. The repeatability of B_1^+ mapping was also evaluated where consistent measurements were obtained across three scans at different spatial resolutions for the same subject as shown in Supplementary Fig. 4.

To further validate 3D-EPTI's reliability, a comparison between quantitative parameters provided by 3D-EPTI and those from standard acquisition methods was conducted *in vivo*. The well-established standard methods provide high quality quantitative parameters at a cost of impractically long acquisition time and therefore a higher level of susceptibility to motion induced artifacts. To mitigate this issue in our comparison, we reduced the spatial resolution ($2 \times 2 \times 3$ mm^3) as well as the slice coverage of the standard acquisitions for T_1 and T_2 to keep them to an acceptable total acquisition time of 53 minutes (note that T_2* acquisition was acquired at matched resolution of isotropic 1-mm). For 3D-EPTI, a single 3-minute scan at 1-mm isotropic resolution with whole brain coverage was used to obtain all the quantitative estimates. As shown in Fig. 5, T_1 measurements of 3D-EPTI and the standard method show high positive correlation (PCC = 0.972, P < 0.0001), with a bias of −7.23% (P < 0.0001). T_2 measurements also show positive correlation (PCC = 0.790, P = 0.0008) with no significant bias (P = 0.1351). Lastly, T_2* values are also highly correlated (PCC = 0.948, p < 0.0001) with a small bias of 4.68% (P = 0.0137). In addition to the in-vivo validation, a phantom experiment was also performed, where the quantitative measurements from 3D-EPTI are in good agreement (PCC = 0.993 for T_1, 0.993 for T_2 and 0.988 for T_2*) with the standard methods in a wide range of quantitative values (Supplementary Fig. 5).

3.3. Ultra-fast 1-min scan and submillimeter mapping enabled by the high efficiency

In addition to the 3-minute 3D-EPTI protocol at 1-mm isotropic resolution, two additional whole-brain protocols at different resolutions were developed to show the high efficiency of 3D-EPTI. An ultra-fast 1-minute protocol at 1.5-mm isotropic resolution obtains high quality quantitative maps as shown in the left panels of Fig. 6 (T_1 map) and Fig. 7 (T_2 and T_2* maps), and a 9-minute protocol at 0.7-mm isotropic resolution protocol allows visualization and evaluation of more detailed brain structures (Fig. 6&7, right panels).

Here, using the high-resolution protocol, we explored the feasibility of using 3D-EPTI to assess intra-cortical structures of healthy volunteers, evaluated its inter-scan and inter-subject repeatability, and explored its potential to identify specific spatial features. Fig. 8a shows the quantitative maps of all the three parameters at different cortical depths from inner (GM-WM) to outer (GM-CSF) surface of a healthy volunteer. Consistent profiles across layers can be observed with distinctly lower values in areas that are highly myelinated, such as areas in motor, sensory, auditory, MT and visual cortex, which are in accordance with previous literatures (Carey et al., 2018; Glasser et al., 2014; Haast et al., 2016; Lutti et al., 2014; Marques et al., 2017). For all the three relaxation parameters, there is a general increasing trend across cortical layers from inner to outer surface, potentially reflecting the decrease of myelin and iron contents from the white matter surface to the CSF surface that has been validated in histological studies (Annese et al., 2004). Fig. 8b shows an example of such profile within a representative ROI in the motor cortex (BA 4a), where consistent profiles from 4 healthy volunteers (color-coded) across two repeated scans (solid and dashed lines) are plotted, showing high inter-scan (intra-subject) and inter-subject repeatability. The repeatability was also measured in other representative ROIs as shown in Fig 8d and 8e, quantified by both the root mean square error (RMSE) and PCC, which assess the differences and the similarities of the cortical profiles among subjects and between scans. The intra-subject profiles were measured with median RMSEs at 20.36 ms, 1.84 ms and 2.94

ms for T_1, T_2, T_2* and median PCCs at 0.999, 0.999 and 0.992. The inter-subject profiles show higher variability than intra-subject as expected, with median RMSEs at 38.47 ms, 4.37 ms and 4.42 ms and median PCCs at 0.998, 0.995, 0.988 for T_1, T_2, T_2* respectively.

Despite the consistency across scans and subjects, the cortical profiles differ across different cortical regions. The average profiles in Fig. 8c revealed different slopes and global values in different ROIs. The results provided by 3D-EPTI in a dramatically reduced scan time agree well with previous literatures that investigated T_1 or T_2* cortical profiles (Carey et al., 2018; Marques et al., 2017; Waehnert et al., 2016). For example, areas such as BA4p in motor cortex and BA3b in sensory cortex have globally lower T_1 profiles than other areas, which might reflect their higher myelin concentration. A relative flat T_2* profile was observed in the visual cortex, which was also reported previously (Carey et al., 2018; Marques et al., 2017) and might be attributed to the highly myelinated middle layers and increasing susceptibility in the outer layers due to presence of blood vessels with a high level of iron. Investigating T_2 profiles across cortical depths have been challenging due to the need for prohibitively long acquisitions. Using 3D-EPTI, different T_2 profiles were also obtained in different ROIs, which could reflect differences in both myelin water content and iron composition and complementary to the findings in T_1 and T_2*.

3.4. High quality synthetic images

Fig. 9a demonstrates the ability of 3D-EPTI for synthetic imaging using its co-registered quantitative maps in several examples, including synthesizing clinical routine contrasts (MPRAGE, T_2-FLAIR and T_2-weighted), and other advanced contrasts such as double inversion recovery (DIR) with better visualization for cortical areas (Calabrese et al., 2007; Wattjes et al., 2007). The high efficiency of 3D-EPTI allows for higher spatial resolution within clinical acceptable time, which can reduce the partial volume effects commonly observed in synthetic images (e.g., the 0.7-mm data shows minimal partial volume effects in challenging FLAIR contrast compared to the 1-mm and 1.5-mm data). Fig. 9b further shows the high resolution of the synthesized DIR images in different views. In Fig. 9c, the spectrums of contrast difference between tissue pairs (gray-white and gray-CSF) were shown, and the selected images with the maximal differences were presented for improved visualization of the image contrast.

4. Discussion

The goal of this study is to address the longstanding problem in quantitative MRI — the slow acquisition speed. To achieve rapid quantitative MRI, 3D-EPTI exploits the spatiotemporal correlation at multiple timescales through new encoding strategies within and between efficient continuous readouts. It enables acquisition of robust multi-parametric maps within minutes at high isotropic resolution with whole brain coverage. As a proof-of-concept, a 3D-EPTI sequence for simultaneous T_1, T_2 and T_2* mapping was developed and validated.

The reliability of the quantitative measures obtained using 3D-EPTI was validated by comparing them to lengthy standard acquisitions, where a generally high level of agreement was observed in both in-vivo (Fig. 5) and phantom (Supplementary Fig. 5) experiments. The

largest difference was observed in the in-vivo T_1-values, with a bias level of 7.23%. This could potentially be attributed to the magnetization transfer (MT) effect, which causes a different level of exchange between water and macromolecular pools in different sequences. This can create discrepancies between the actual and the modeled signal evolutions in both 3D-EPTI and in the standard acquisition, where the MT effect has not been accounted for. 3D-EPTI uses long continuous readouts and therefore fewer RF pulses, which could reduce the RF duty cycle and the corresponding MT effect than other sequences with high RF duty cycles. However, the MT effect can still affect the quantification accuracy in this study especially for T_1 due to the use of the inversion recovery pulse. The characterization and disentanglement of the MT effect in quantitative mapping is an active area of research (Hilbert et al., 2020). Future work will investigate the incorporation of a MT-sensitive sequence module into the 3D-EPTI acquisition, and model the MT effect in both the reconstruction and the parameter fitting. The simulation test (Supplementary Fig. 3) compares 3D-EPTI with gold-standard simulated data, and demonstrates the accuracy of its reconstruction and quantification in an ideal case (without MT effect). In the simulation test, white and gray matter regions result in low level of errors, while CSF shows higher errors as expected due to its high baseline values (long T_1, T_2, T_2*). In addition, the lower accuracy of CSF especially for T_2* (higher percentage error) might be attributed to the fact that the protocols used in this study were designed to be optimized for the tissues of interest (gray and white matter) with a limited TE range, therefore have compromised capability to accurately estimate long values.

The intra- and inter-subject repeatability of the quantitative parameters obtained by 3D-EPTI was demonstrated across multiple healthy volunteers. High intra-subject repeatability was observed, which will be critical to the success of future deployment of 3D-EPTI to various applications such as in longitudinal monitoring of healthy and diseased tissues during complex biological process of brain development or pathophysiological progression of neurological diseases. Nonetheless, despite our efforts to minimize the bias in the repeatability assessment process itself, such as by using automatically segmented ROIs instead of manually-selected ROIs, the small variations (COV < 2.27%) could still be partially caused by errors in the registration process to align the two scans for comparison. Moreover, inherent differences between scans are possible. For example, T_2* shows higher variability than T_1 and T_2 (Fig. 4c), which could be reflective of the variability in the head position between the scan and rescan acquisitions, where previous findings have demonstrated variability in T_2* values as a function of head orientation relative to the main field (Cohen-Adad et al., 2012). The higher variability in CSF and deep brain regions (Fig. 4d) might be caused by the higher g-factor (worse coil sensitivity) and physiological noise. The high inter-subject repeatability (COV < 5.09%) of the quantitative parameters points to the potential of 3D-EPTI for use in establishing population-average norms or atlases. On the other hand, the inter-subject repeatability is lower than the intra-subject repeatability as expected. This could reflect its ability to detect inherent individual differences. However, some of the increased variability could also be attributed to the additional segmentation variabilities across subjects.

The high efficiency of 3D-EPTI enables the simultaneous acquisition of T_1, T_2, T_2* at submillimeter resolution within a few minutes for the first time. The high isotropic

resolution should be particularly helpful in studying detailed brain structures, such as the intra-cortical architecture with different levels of myelination or iron concentration (Carey et al., 2018; Haast et al., 2016; Lutti et al., 2014; Marques et al., 2017; Trampel et al., 2019; Waehnert et al., 2016; Warntjes et al., 2016). In this study, high intra- and inter-subject repeatability were observed in the intra-cortical profiles obtained by 3D-EPTI, preliminarily demonstrating the robust performance in using 3D-EPTI data to conduct reliable surface reconstruction and reveal repeatable subtle features across cortical layers.

The concept of 3D-EPTI can be readily adopted to other pulse sequences for quantification of other tissue parameters. For example, 3D-EPTI should be well suited for parameter estimation of multiple-pool models (Dong et al., 2021a), because it can continuously track complex signal evolutions at a short time scale to offer more degrees of freedom in estimating these parameters. The unique features of 3D-EPTI also open up many possibilities for further technical improvements. For example, the radial pattern of the block-wise sampling of 3D-EPTI allows for robust motion correction between repetitions (Dong et al., 2021b). Other advanced reconstruction algorithms, including machine learning and multi-dimensional low-rank tensor approach (Christodoulou et al., 2018; Liang, 2007), may further improve the accuracy of time-resolving reconstruction. The adaptation of EPTI to non-Cartesian acquisitions can also help eliminate their potential distortion/blurring artifacts due to the long readouts and provide multi-contrast capability (Fair et al., 2020; Liberman et al., 2020a, b). The high-resolution acquisition of 3D-EPTI can reduce the partial-volume effect of synthetic images. Machine learning based approaches can be applied to directly synthesize images from the multi-contrast images or subspace coefficient maps of the 3D-EPTI data, which may further mitigate the partial-volume effect (Qiu et al., 2021; Wang et al., 2020).

To summarize, we introduce a novel method, termed 3D-Echo Planar Time-Resolved Imaging (3D-EPTI), that enables high acceleration and significantly improved imaging efficiency for multi-parametric imaging. By pushing multi-parametric MRI into a faster regime, 3D-EPTI may help improve quantitative imaging in future applications (e.g., reducing the chance of involuntary movements), and also open up the possibility of acquiring multi-parametric maps at submillimeter isotropic resolution within a few minutes to reveal more detailed brain structures for neuroscientific research.

Supplementary Material

Refer to Web version on PubMed Central for supplementary material.

Acknowledgments

possible by the resources provided by NIH Shared Instrumentation Grants S10-RR023401, S10-RR023043, and S10-RR019307.

Data and Code Availability Statement

Example de-identified datasets supporting the results, and example raw k-space data for subspace reconstruction are available at https://doi.org/10.6084/m9.figshare.14558154. Example MATLAB code of the subspace reconstruction are available at: https://github.com/Fuyixue/3D-EPTI.

References

Annese J, Pitiot A, Dinov ID, Toga AW, 2004. A myelo-architectonic method for the structural classification of cortical areas. Neuroimage 21, 15–26. [PubMed: 14741638]

Bernasconi N, Bernasconi A, Andermann F, Dubeau F, Feindel W, Reutens DC, 1999. Entorhinal cortex in temporal lobe epilepsy: a quantitative MRI study. Neurology 52, 1870–1876. [PubMed: 10371536]

Boyacioglu R, Wang C, Ma D, McGivney DF, Yu X, Griswold MA, 2021. 3D magnetic resonance fingerprinting with quadratic RF phase. Magn. Reson. Med 85, 2084–2094. [PubMed: 33179822]

Boyd S, Parikh N, Chu E, Peleato B, Eckstein J, 2011. Distributed optimization and statistical learning via the alternating direction method of multipliers. Faund. Trends Mach. Learn 3, 1–122.

Bozzali M, Serra L, Cercignani M, 2016. Quantitative MRI to understand Alzheimer's disease pathophysiology. Curr. Opin. Neurol 29, 437–444. [PubMed: 27228309]

Breuer FA, Blaimer M, Heidemann RM, Mueller MF, Griswold MA, Jakob PM, 2005. Controlled aliasing in parallel imaging results in higher acceleration (CAIPIR-INHA) for multi-slice imaging. Magn. Reson. Med 53, 684–691. [PubMed: 15723404]

Breuer FA, Blaimer M, Mueller MF, Seiberlich N, Heidemann RM, Griswold MA, Jakob PM, 2006. Controlled aliasing in volumetric parallel imaging (2D CAIPIR-INHA). Magn. Reson. Med 55, 549–556. [PubMed: 16408271]

Buonincontri G, Biagi L, Retico A, Cecchi P, Cosottini M, Gallagher FA, Gómez PA, Graves MJ, McLean MA, Riemer F, 2019. Multi-site repeatability and reproducibility of MR fingerprinting of the healthy brain at 1.5 and 3.0 T. Neuroimage 195, 362–372. [PubMed: 30923028]

Caan MW, Bazin PL, Marques JP, de Hollander G, Dumoulin SO, van der Zwaag W, 2019. MP2RAGEME: T1, T2*, and QSM mapping in one sequence at 7tesla. Hum. Brain Mapp 40, 1786–1798. [PubMed: 30549128]

Calabrese M, De Stefano N, Atzori M, Bernardi V, Mattisi I, Barachino L, Morra A, Rinaldi L, Romualdi C, Perini P, 2007. Detection of cortical inflammatory lesions by double inversion recovery magnetic resonance imaging in patients with multiple sclerosis. Arch. Neurol 64, 1416–1422. [PubMed: 17923625]

Carey D, Caprini F, Allen M, Lutti A, Weiskopf N, Rees G, Callaghan MF, Dick F, 2018. Quantitative MRI provides markers of intra-, inter-regional, and age-related differences in young adult cortical microstructure. Neuroimage 182, 429–440. [PubMed: 29203455]

Christodoulou AG, Shaw JL, Nguyen C, Yang Q, Xie Y, Wang N, Li D, 2018. Magnetic resonance multitasking for motion-resolved quantitative cardiovascular imaging. Nat. Biomed. Eng 2, 215–226. [PubMed: 30237910]

Cloos MA, Knoll F, Zhao T, Block KT, Bruno M, Wiggins GC, Sodickson DK, 2016. Multiparametric imaging with heterogeneous radiofrequency fields. Nat. Commun 7, 12445. [PubMed: 27526996]

Cohen O, Polimeni JR, 2018. Optimized inversion-time schedules for quantitative T1 measurements based on high-resolution multi-inversion EPI. Magn. Reson. Med 79, 2101–2112. [PubMed: 28845547]

Cohen-Adad J, Polimeni JR, Helmer KG, Benner T, McNab JA, Wald LL, Rosen BR, Mainero C, 2012. T2* mapping and B0 orientation-dependence at 7 T reveal cyto-and myeloarchitecture organization of the human cortex. Neuroimage 60, 1006–1014. [PubMed: 22270354]

Deoni SC, Rutt BK, Peters TM, 2003. Rapid combined T1 and T2 mapping using gradient recalled acquisition in the steady state. Magn. Reson. Med 49, 515–526. [PubMed: 12594755]

Desikan RS, Segonne F, Fischl B, Quinn BT, Dickerson BC, Blacker D, Buckner RL, Dale AM, Maguire RP, Hyman BT, Albert MS, Killiany RJ, 2006. An automated labeling system for subdividing the human cerebral cortex on MRI scans into gyral based regions of interest. Neuroimage 31, 968–980. [PubMed: 16530430]

Dong Z, Wang F, Chan K-S, Reese TG, Bilgic B, Marques JP, Setsompop K, 2021a. Variable flip angle echo planar time-resolved imaging (vFA-EPTI) for fast high-resolution gradient echo myelin water imaging. Neuroimage 232, 117897. [PubMed: 33621694]

Dong Z, Wang F, Reese TG, Bilgic B, Setsompop K, 2020. Echo planar time-resolved imaging with subspace reconstruction and optimized spatiotemporal encoding. Magn. Reson. Med 84, 2442–2455. [PubMed: 32333478]

Dong Z, Wang F, Reese TG, Manhard MK, Bilgic B, Wald LL, Guo H, Setsompop K, 2019. Tilted-CAIPI for highly accelerated distortion-free EPI with point spread function (PSF) encoding. Magn. Reson. Med 81, 377–392. [PubMed: 30229562]

Dong Z, Wang F, Xiang J, Setsompop K, 2021b. Motion-corrected 3D-EPTI with 4D navigatorfor fast and robust whole-brain quantitative imaging. In: Proceedings of the 29th Annual Meeting of ISMRM, p. 0119.

Fair MJ, Wang F, Dong Z, Reese TG, Setsompop K, 2020. Propeller echo-planar time-resolved imaging with dynamic encoding (PEPTIDE). Magn. Reson. Med 83, 2124–2137. [PubMed: 31703154]

Falangola M, Dyakin V, Lee S, Bogart A, Babb J, Duff K, Nixon R, Helpern, 2007. Quantitative MRI reveals aging-associated T2 changes in mouse models of Alzheimer's disease. NMR Biomed 20, 343–351. [PubMed: 17451178]

Feinberg DA, Oshio K, 1991. GRASE (gradient-and spin-echo) MR imaging: a new fast clinical imaging technique. Radiology 181, 597–602. [PubMed: 1924811]

Filo S, Shtangel O, Salamon N, Kol A, Weisinger B, Shifman S, Mezer AA, 2019. Disentangling molecular alterations from water-content changes in the aging human brain using quantitative MRI. Nat. Commun 10, 1–16. [PubMed: 30602773]

Fischl B, 2012. FreeSurfer. Neuroimage 62, 774–781. [PubMed: 22248573]

Fischl B, Salat DH, Busa E, Albert M, Dieterich M, Haselgrove C, van der Kouwe A, Killiany R, Kennedy D, Klaveness S, Montillo A, Makris N, Rosen B, Dale AM, 2002. Whole brain segmentation: automated labeling of neuroanatomical structures in the human brain. Neuron 33, 341–355. [PubMed: 11832223]

Fujita S, Hagiwara A, Hori M, Warntjes M, Kamagata K, Fukunaga I, Andica C, Maekawa T, Irie R, Takemura MY, Kumamaru KK, Wada A, Suzuki M, Ozaki Y, Abe O, Aoki S, 2019. Three-dimensional high-resolution simultaneous quantitative mapping of the whole brain with 3D-QALAS: An accuracy and repeatability study. Magn. Reson. Imaging 63, 235–243. [PubMed: 31445118]

Glasser MF, Goyal MS, Preuss TM, Raichle ME, Van Essen DC, 2014. Trends and properties of human cerebral cortex: correlations with cortical myelin content. Neuroimage 93, 165–175. [PubMed: 23567887]

Griswold MA, Jakob PM, Heidemann RM, Nittka M, Jellus V, Wang J, Kiefer B, Haase A, 2002. Generalized autocalibrating partially parallel acquisitions (GRAPPA). Magn. Reson. Med 47, 1202–1210. [PubMed: 12111967]

Guo R, Zhao Y, Li Y, Wang T, Li Y, Sutton B, Liang ZP, 2021. Simultaneous QSM and metabolic imaging of the brain using SPICE: Further improvements in data acquisition and processing. Magn. Reson. Med 85, 970–977. [PubMed: 32810319]

Haast RA, Ivanov D, Formisano E, Uluda K, 2016. Reproducibility and reliability of quantitative and weighted T1 and T2* mapping for myelin-based cortical parcellation at 7 Tesla. Front. Neuroanatomy 10, 112.

He J, Liu Q, Christodoulou AG, Ma C, Lam F, Liang ZP, 2016. Accelerated High-Dimensional MR Imaging With Sparse Sampling Using Low-Rank Tensors. IEEE Trans. Med. Imaging 35, 2119–2129. [PubMed: 27093543]

Hilbert T, Xia D, Block KT, Yu Z, Lattanzi R, Sodickson DK, Kober T, Cloos MA, 2020. Magnetization transfer in magnetic resonance fingerprinting. Magn. Reson. Med 84, 128–141. [PubMed: 31762101]

Hong T, Han D, Kim DH, 2019. Simultaneous estimation of PD, T1, T2, T2*, and B0 using magnetic resonance fingerprinting with background gradient compensation. Magn. Reson. Med 81, 2614–2623. [PubMed: 30426568]

Jenkinson M, Bannister P, Brady M, Smith S, 2002. Improved optimization for the robust and accurate linear registration and motion correction of brain images. Neuroimage 17, 825–841. [PubMed: 12377157]

Jenkinson M, Beckmann CF, Behrens TE, Woolrich MW, Smith SM, 2012. Fsl. Neuroimage 62, 782–790. [PubMed: 21979382]

Jenkinson M, Smith S, 2001. A global optimisation method for robust affine registration of brain images. Med. Image Anal 5, 143–156. [PubMed: 11516708]

Jiang Y, Ma D, Seiberlich N, Gulani V, Griswold MA, 2015. MR fingerprinting using fast imaging with steady state precession (FISP) with spiral readout. Magn. Reson. Med 74, 1621–1631. [PubMed: 25491018]

Krauss W, Gunnarsson M, Andersson T, Thunberg P, 2015. Accuracy and reproducibility of a quantitative magnetic resonance imaging method for concurrent measurements of tissue relaxation times and proton density. Magn. Reson. Imaging 33, 584–591. [PubMed: 25708264]

Lam F, Liang ZP, 2014. A subspace approach to high-resolution spectroscopic imaging. Magn. Reson. Med 71, 1349–1357. [PubMed: 24496655]

Lescher S, Jurcoane A, Veit A, Bahr O, Deichmann R, Hattingen E, 2015. Quantitative T1 and T2 mapping in recurrent glioblastomas under bevacizumab: earlier detection of tumor progression compared to conventional MRI. Neuroradiology 57, 11–20. [PubMed: 25287076]

Liang Z-P, 2007. Spatiotemporal imagingwith partially separable functions. In: 2007 4th IEEE International Symposium on Biomedical Imaging: From Nano to Macro. IEEE, pp. 988–991.

Liao C, Bilgic B, Manhard MK, Zhao B, Cao X, Zhong J, Wald LL, Setsompop K, 2017. 3D MR fingerprinting with accelerated stack-of-spirals and hybrid sliding-window and GRAPPA reconstruction. Neuroimage 162, 13–22. [PubMed: 28842384]

Liberman G, Wang F, Dong Z, Setsompop K, 2020a. Flexible model-based reconstruction through generalized cycled parameter splitting approach. In: Proceedings of the 29th Annual Meeting of ISMRM, p. 0884.

Liberman G, Wang F, Dong Z, Setsompop K, 2020b. Spiral crisscrossing echo planar time-resolved imaging (SCEPTI). In: Proceedings of the 29th Annual Meeting of ISMRM, p. 0616.

Lustig M, Donoho D, Pauly JM, 2007. Sparse MRI: The application of compressed sensing for rapid MR imaging. Magn. Reson. Med 58, 1182–1195. [PubMed: 17969013]

Lutti A, Dick F, Sereno MI, Weiskopf N, 2014. Using high-resolution quantitative mapping of R1 as an index of cortical myelination. Neuroimage 93, 176–188. [PubMed: 23756203]

Ma D, Gulani V, Seiberlich N, Liu K, Sunshine JL, Duerk JL, Griswold MA, 2013. Magnetic resonance fingerprinting. Nature 495, 187–192. [PubMed: 23486058]

Ma D, Jiang Y, Chen Y, McGivney D, Mehta B, Gulani V, Griswold M, 2018a. Fast 3D magnetic resonance fingerprinting for a whole-brain coverage. Magn. Reson. Med 79, 2190–2197. [PubMed: 28833436]

Ma D, Jones SE, Deshmane A, Sakaie K, Pierre EY, Larvie M, McGivney D, Blümcke I, Krishnan B, Lowe M, 2018b. Development of high-resolution 3D MR fingerprinting for detection and characterization of epileptic lesions. J. Magn. Reson. Imaging 49, 1333–1346. [PubMed: 30582254]

Ma S, Nguyen CT, Han F, Wang N, Deng Z, Binesh N, Moser FG, Christodoulou AG, Li D, 2020. Three-dimensional simultaneous brain T1, T2, and ADC mapping with MR Multitasking. Magn. Reson. Med 84, 72–88. [PubMed: 31765496]

Ma S, Wang N, Fan Z, Kaisey M, Sicotte NL, Christodoulou AG, Li D, 2021. Three-dimensional whole-brain simultaneous T1, T2, and T1ρ quantification using MR Multitasking: Method and initial clinical experience in tissue characterization of multiple sclerosis. Magn. Reson. Med 85, 1938–1952. [PubMed: 33107126]

Mansfield P, 1977. Multi-planar image-formation using Nmr spin echoes. J. Phys C 10, L55–L58.

Marques JP, Khabipova D, Gruetter R, 2017. Studying cyto and myeloarchitecture of the human cortex at ultra-high field with quantitative imaging: R1, R2* and magnetic susceptibility. Neuroimage 147, 152–163. [PubMed: 27939794]

Meng Z, Guo R, Li Y, Guan Y, Wang T, Zhao Y, Sutton B, Li Y, Liang ZP, 2021. Accelerating T2 mapping of the brain by integrating deep learning priors with low-rank and sparse modeling. Magn. Reson. Med 85, 1455–1467. [PubMed: 32989816]

Metere R, Kober T, Möller HE, Schäfer A, 2017. Simultaneous quantitative MRI mapping of T1, T2* and magnetic susceptibility with multi-echo MP2RAGE. PLoS One 12, e0169265. [PubMed: 28081157]

Müller A, Jurcoane A, Kebir S, Ditter P, Schrader F, Herrlinger U, Tzaridis T, Mädler B, Schild HH, Glas M, 2017. Quantitative T1-mapping detects cloudy-enhancing tumor compartments predicting outcome of patients with glioblastoma. Cancer Med 6, 89–99. [PubMed: 27891815]

Oshio K, Feinberg DA, 1991. GRASE (gradient-and spin-echo) imaging: a novel fast MRI technique. Magn. Reson. Med 20, 344–349. [PubMed: 1775061]

Pruessmann KP, Weiger M, Scheidegger MB, Boesiger P, 1999. SENSE: sensitivity encoding for fast MRI. Magn. Reson. Med 42, 952–962. [PubMed: 10542355]

Qiu S, Chen Y, Ma S, Fan Z, Christodoulou AG, Xie Y, li D, 2021. Direct synthesis of multi-contrast images from MR multitasking spatial factors using deep learning. Proc. Int. Soc. Mag. Reson. Med 2429.

Ramani A, Jensen JH, Helpern JA, 2006. Quantitative MR imaging in Alzheimer disease. Radiology 241, 26–44. [PubMed: 16990669]

Reitz SC, Hof SM, Fleischer V, Brodski A, Groger A, Gracien RM, Droby A, Steinmetz H, Ziemann U, Zipp F, Deichmann R, Klein JC, 2017. Multi-parametric quantitative MRI of normal appearing white matter in multiple sclerosis, and the effect of disease activity on T2. Brain Imaging Behav 11, 744–753. [PubMed: 27138529]

Sled JG, Nossin-Manor R, 2013. Quantitative MRI for studying neonatal brain development. Neuroradiology 55 (Suppl 2), 97–104. [PubMed: 23872867]

Sodickson DK, Manning WJ, 1997. Simultaneous acquisition of spatial harmonics (SMASH): fast imaging with radiofrequency coil arrays. Magn. Reson. Med 38, 591–603. [PubMed: 9324327]

Tamir JI, Ong F, Cheng JY, Uecker M, Lustig M, 2016. Generalized magnetic resonance image reconstruction using the Berkeley advanced reconstruction toolbox. ISMRM Workshop on Data Sampling & Image Reconstruction.

Tamir JI, Uecker M, Chen W, Lai P, Alley MT, Vasanawala SS, Lustig M, 2017. T2 shuffling: sharp, multicontrast, volumetric fast spin-echo imaging. Magn. Reson. Med 77, 180–195. [PubMed: 26786745]

Tardif CL, Bedell BJ, Eskildsen SF, Collins DL, Pike GB, 2011. Quantitative magnetic resonance imaging of cortical multiple sclerosis pathology. Mult. Scler. Int 2012.

Tofts P, 2005. Quantitative MRI of the Brain: Measuring Changes Caused by Disease John Wiley & Sons.

Trampel R, Bazin PL, Pine K, Weiskopf N, 2019. In-vivo magnetic resonance imaging (MRI) of laminae in the human cortex. Neuroimage 197, 707–715. [PubMed: 28942063]

Trzasko J, Manduca A, Borisch E, 2011. Local versus global low-rank promotion in dynamic MRI series reconstruction. Proc. Int. Symp. Magn. Reson. Med 4371.

Uecker M, Ong F, Tamir JI, Bahri D, Virtue P, Cheng JY, Zhang T, Lustig M, 2015. Berkeley advanced reconstruction toolbox. Proc. Intl. Soc. Mag. Reson. Med.

Waehnert M, Dinse J, Weiss M, Streicher MN, Waehnert P, Geyer S, Turner R, Bazin P-L, 2014. Anatomically motivated modeling of cortical laminae. Neuroimage 93, 210–220. [PubMed: 23603284]

Waehnert MD, Dinse J, Schafer A, Geyer S, Bazin PL, Turner R, Tardif CL, 2016. A subject-specific framework for in vivo myeloarchitectonic analysis using high resolution quantitative MRI. Neuroimage 125, 94–107. [PubMed: 26455795]

Wang F, Dong Z, Reese TG, Bilgic B, Katherine Manhard M, Chen J, Polimeni JR, Wald LL, Setsompop K, 2019a. Echo planar time-resolved imaging (EPTI). Magn. Reson. Med 81, 3599–3615. [PubMed: 30714198]

Wang F, Dong Z, Reese TG, Wald LL, Setsompop K, 2019b. 3D-EPTI for ultra-fast multi-contrast and quantitative imaging. Proc. Int. Soc. Mag. Reson. Med p944.

Wang F, Dong Z, Wald LL, Polimeni JR, Setsompop K, 2021. Simultaneous pure T2 and varying T2′-weighted BOLD fMRI using Echo Planar Time-resolved Imaging for mapping cortical-depth dependent responses. Neuroimage 245, 118641. [PubMed: 34655771]

Wang K, Doneva M, Amthor T, Keil VC, Karasan E, Tan F, Tamir JI, Yu SX, Lustig M, 2020. High fidelity direct-contrast synthesis from magnetic resonance fingerprinting in diagnostic imaging. In: Proceedings of the 28th Annual Meeting of ISMRM, p. 867.

Warntjes JB, Dahlqvist O, Lundberg P, 2007. Novel method for rapid, simultaneous T1, T2*, and proton density quantification. Magn. Reson. Med 57, 528–537. [PubMed: 17326183]

Warntjes JB, Leinhard OD, West J, Lundberg P, 2008. Rapid magnetic resonance quantification on the brain: Optimization for clinical usage. Magn. Reson. Med 60, 320–329. [PubMed: 18666127]

Warntjes M, Engstrom M, Tisell A, Lundberg P, 2016. Modeling the presence of myelin and edema in the brain based on multi-parametric quantitative MRI. Front. Neurol 7, 16. [PubMed: 26925030]

Wattjes M, Lutterbey G, Gieseke J, Träber F, Klotz L, Schmidt S, Schild H, 2007. Double inversion recovery brain imaging at 3T: diagnostic value in the detection of multiple sclerosis lesions. Am. J. Neuroradiol 28, 54–59. [PubMed: 17213424]

Weigel M, 2015. Extended phase graphs: dephasing, RF pulses, and echoes-pure and simple. J. Magn. Reson. Imaging 41, 266–295. [PubMed: 24737382]

West J, Aalto A, Tisell A, Leinhard OD, Landtblom AM, Smedby O, Lundberg P, 2014. Normal appearing and diffusely abnormal white matter in patients with multiple sclerosis assessed with quantitative MR. PLoS One 9, e95161. [PubMed: 24747946]

Wyatt CR, Smith TB, Sammi MK, Rooney WD, Guimaraes AR, 2018. Multi–parametric T2* magnetic resonance fingerprinting using variable echo times. NMR Biomed 31, e3951. [PubMed: 30011109]

Zhang T, Pauly JM, Levesque IR, 2015. Accelerating parameter mapping with a locally low rank constraint. Magn. Reson. Med 73, 655–661. [PubMed: 24500817]

Zhao B, Lu W, Hitchens TK, Lam F, Ho C, Liang ZP, 2015. Accelerated MR parameter mapping with low-rank and sparsity constraints. Magn. Reson. Med 74, 489–498. [PubMed: 25163720]

Zhao B, Setsompop K, Adalsteinsson E, Gagoski B, Ye H, Ma D, Jiang Y, Ellen Grant P, Griswold MA, Wald LL, 2018. Improved magnetic resonance fingerprinting reconstruction with low-rank and subspace modeling. Magn. Reson. Med 79, 933–942. [PubMed: 28411394]
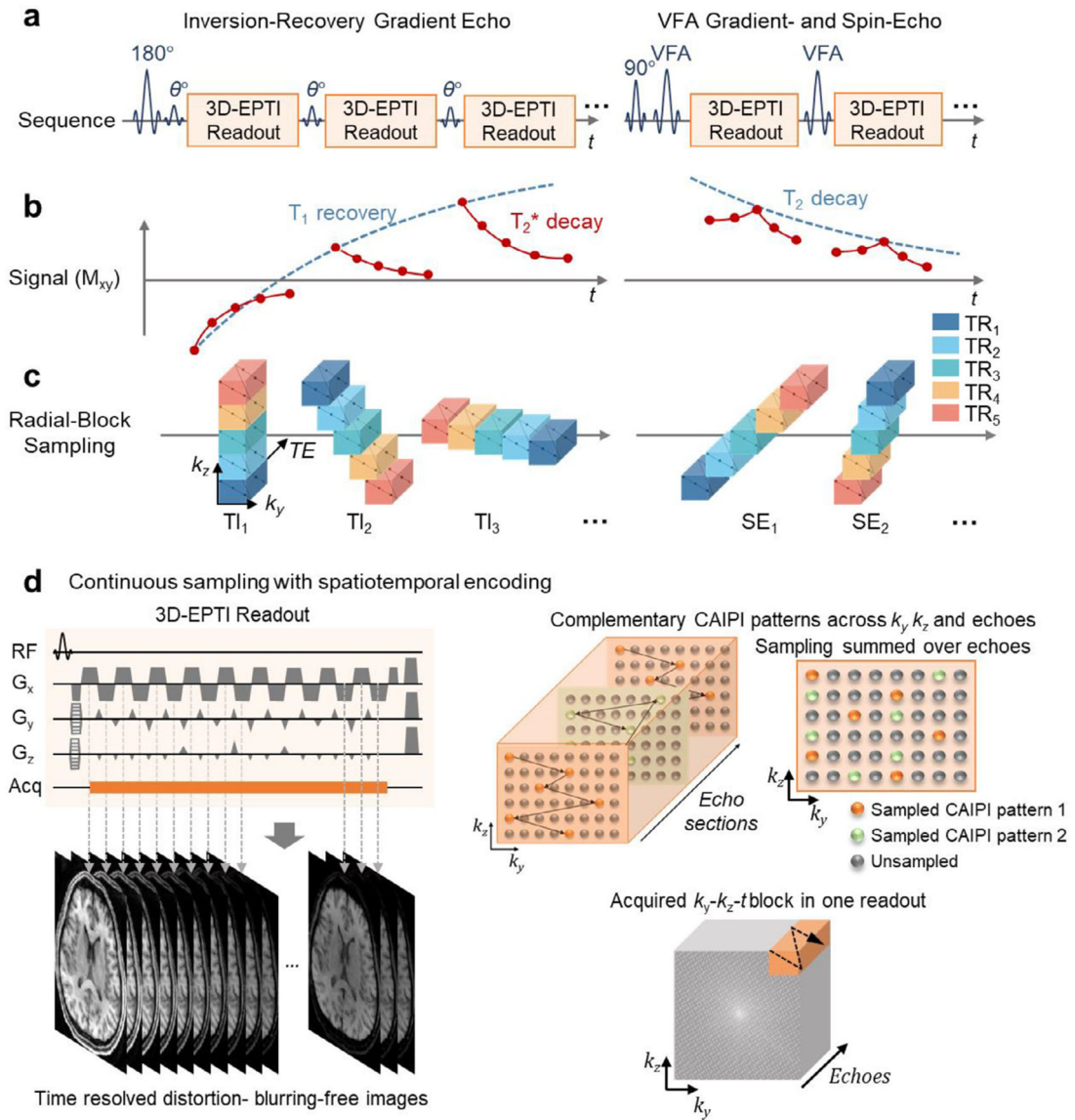
Fig. 1.

Illustration of the 3D-EPTI acquisition. **a**, The sequence diagrams of the inversion-recovery gradient-echo (IR-GE) and the variable-flip-angle gradient and spin-echo (VFA-GRASE) sequences with 3D-EPTI readouts at different inversion times (TI) and spin-echoes (SE). **b**, The designed sequence provides signal evolutions with high sensitivity to T_1, T_2 and T_2^* relaxation time constants, which can be continuously tracked by the 3D-EPTI readouts. **c**, Instead of acquiring the full k_y-k_z space at every TI or SE, a radial-block Cartesian sampling pattern is utilized to quickly sample the k-t space in a small number of TRs. At each TI or SE, the k_y-k_z-t blocks acquired in different TRs (color-coded) form a radial blade with different angulations to create spatiotemporal incoherent aliasing for constrained reconstruction and permit ~10 × acceleration. **d**, Details of the continuous bipolar readout with an optimized spatiotemporal CAIPI encoding used to efficiently cover a k_y-k_z-t block per 3D-EPTI readout. The neighboring data points are acquired close in time to create

high temporal correlation. Two CAIPI patterns (orange and green points) are utilized in a complementary fashion at a longer timescale in different echo sections. The combination of spatiotemporal CAIPI and radial-block undersampling offers ~800 × acceleration in the spatiotemporal domain. Note that the readout (k_x) dimension is fully-sampled and therefore omitted in the illustration.
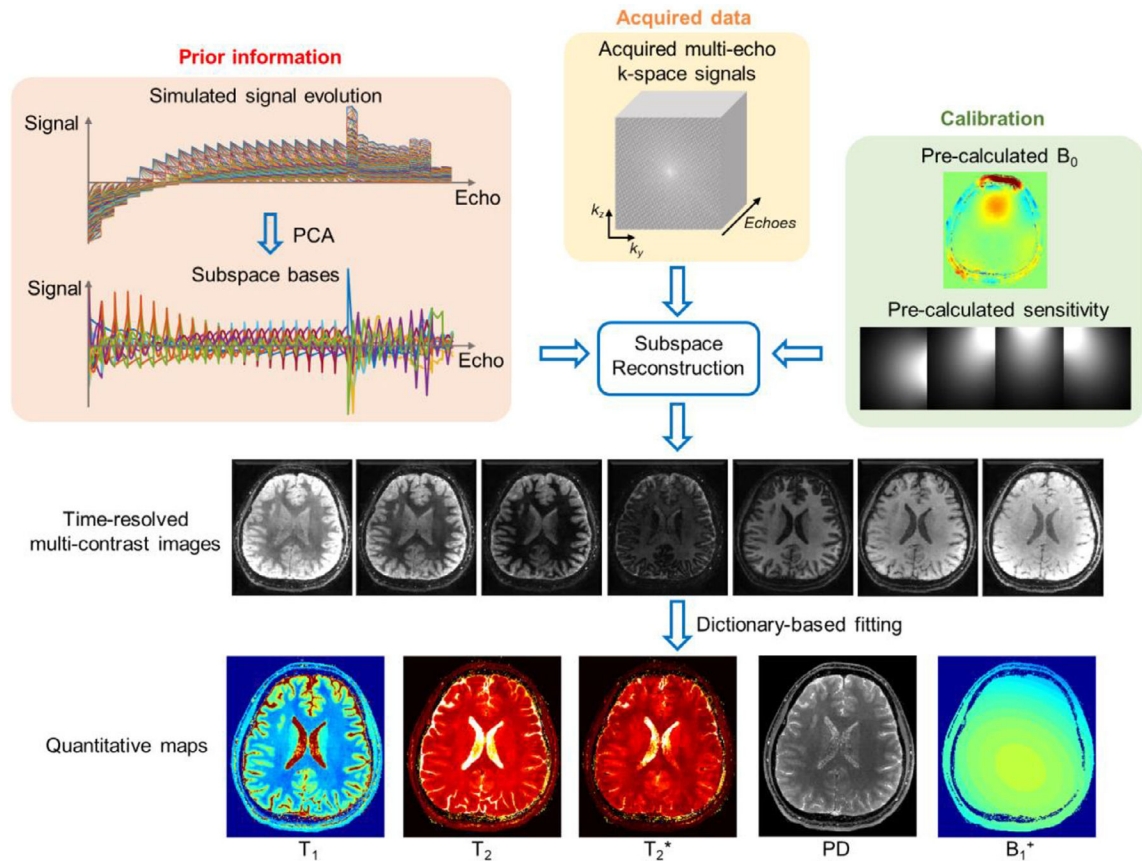
Fig. 2.
Illustration of the reconstruction framework of 3D-EPTI using the low-rank subspace method. The signal evolutions can be represented by a linear combination of several subspace temporal bases, therefore reducing the number of unknowns. The bases are extracted from the simulated signal space using principal component analysis (PCA). The subspace reconstruction is performed by integrating the information from the subspace bases, a highly-undersampled spatiotemporal dataset, and B_0 phase evolution and coil sensitivity maps obtained via a calibration dataset. After the reconstruction, thousands of multi-contrast images can be obtained without distortion and blurring, from which multiple quantitative parameters including T_1, T_2, T_2^*, PD, and B_1^+ can be estimated through dictionary matching.
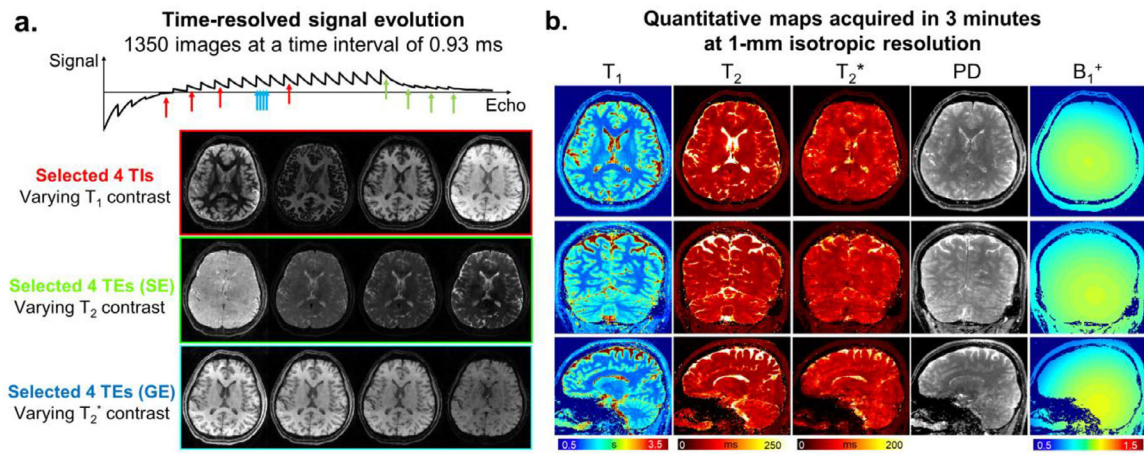
Fig. 3.
Simultaneous whole-brain T_1, T_2 and T_2* mapping at 1-mm isotropic resolution in 3 minutes acquired by 3D-EPTI. **a**, Representative reconstructed multi-contrast images with different T_1, T_2, and T_2* weightings selected from the 1350 resolved images. **b**, High-resolution quantitative maps estimated from the multi-contrast images, including T_1, T_2, T_2*, PD and B_1^+, shown in three orthogonal views.
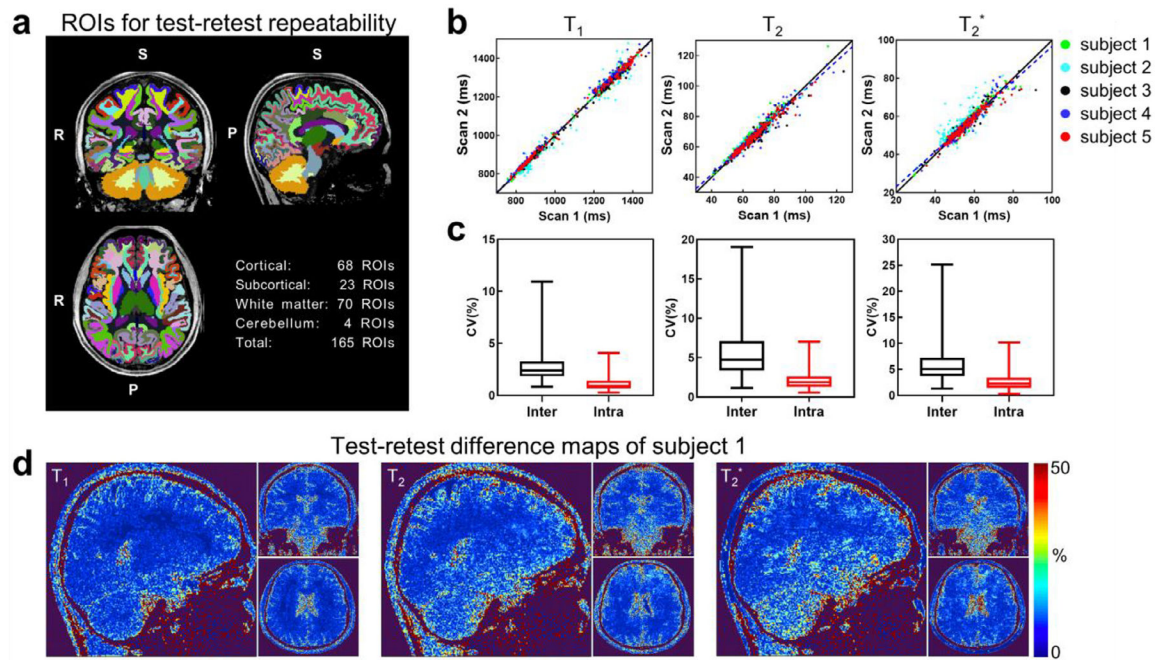
Fig. 4.

Repeatability test of 3D-EPTI for simultaneous T_1, T_2 and T_2^* mapping using the 3-minute 1-mm protocol. **a**, 3D volumes are segmented into 165 ROIs across the whole brain. **b**, Scatter plots of the test-retest T_1, T_2, T_2^* values in the 165 ROIs measured from 5 subjects, shown along with the identity line (solid) and the regressed line (dashed). **c**, Box-plots of the coefficient of variation (COV) between (inter) and within (intra) subjects with whiskers showing minimum and maximum data points. **d**, The percentage difference maps in one of the subjects that show the spatial distribution of the test-retest variations for the 3 parameters.
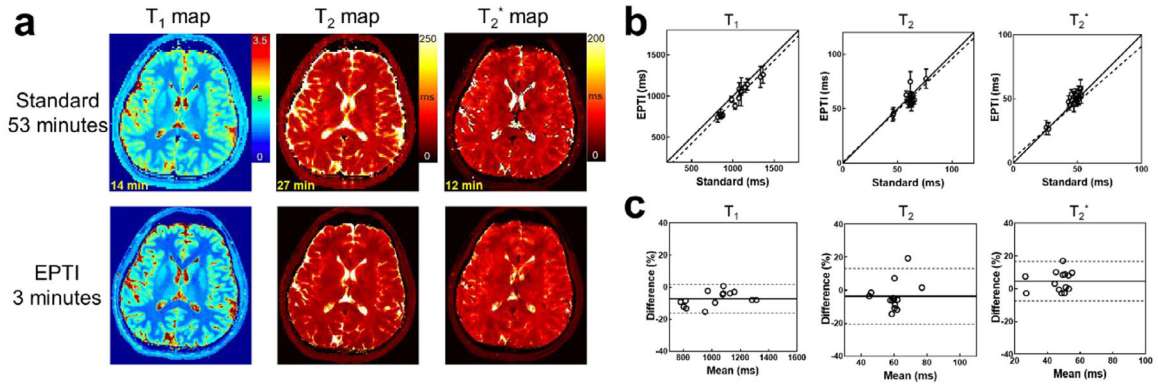
Fig. 5.

Comparison of the quantitative measurements obtained using 3D-EPTI vs. lengthy standard acquisitions *in vivo*. **a**, Quantitative maps acquired by the standard methods and 3D-EPTI. **b**, Scatter plots of the quantitative values from 14 selected ROIs, shown along with the identity line (solid) and the regressed line (dashed). **c**, Bland-Alman plots of the same data with the mean differences or the estimated biases (solid lines) and the 95% limits of agreements (dotted lines).
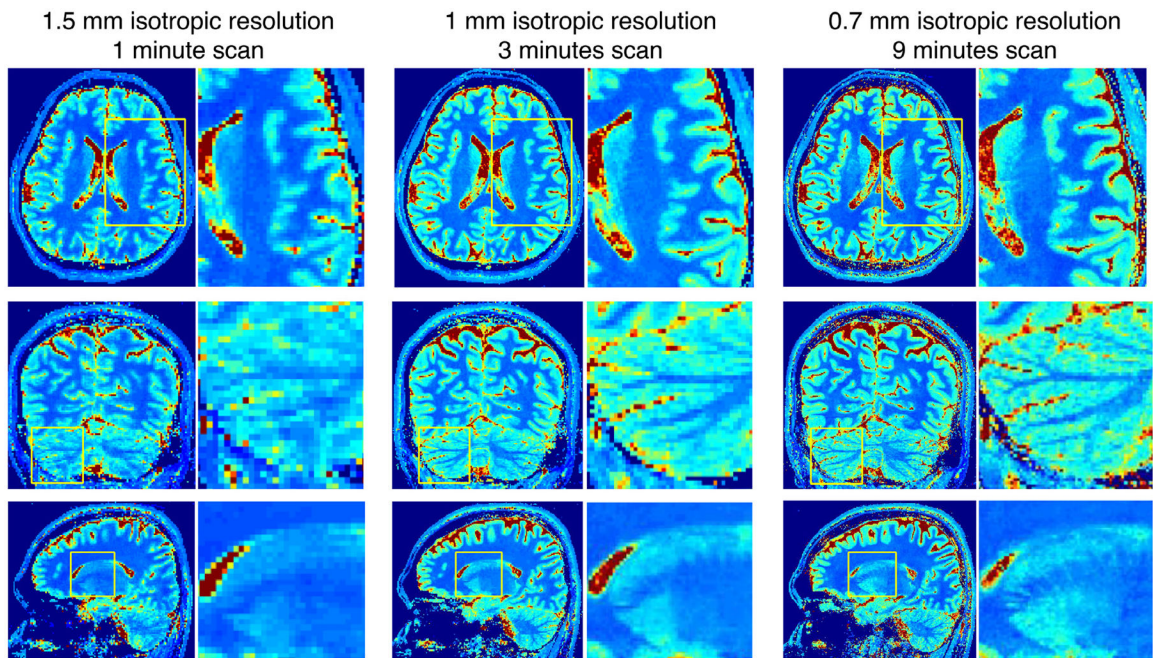
Fig. 6.
Example T_1 maps with zoomed-in areas provided by 3D-EPTI protocols at different spatial resolutions: 1-minute scan at 1.5-mm isotropic resolution, 3-minute scan at 1-mm isotropic resolution, and 9-minute scan at 0.7-mm isotropic resolution.
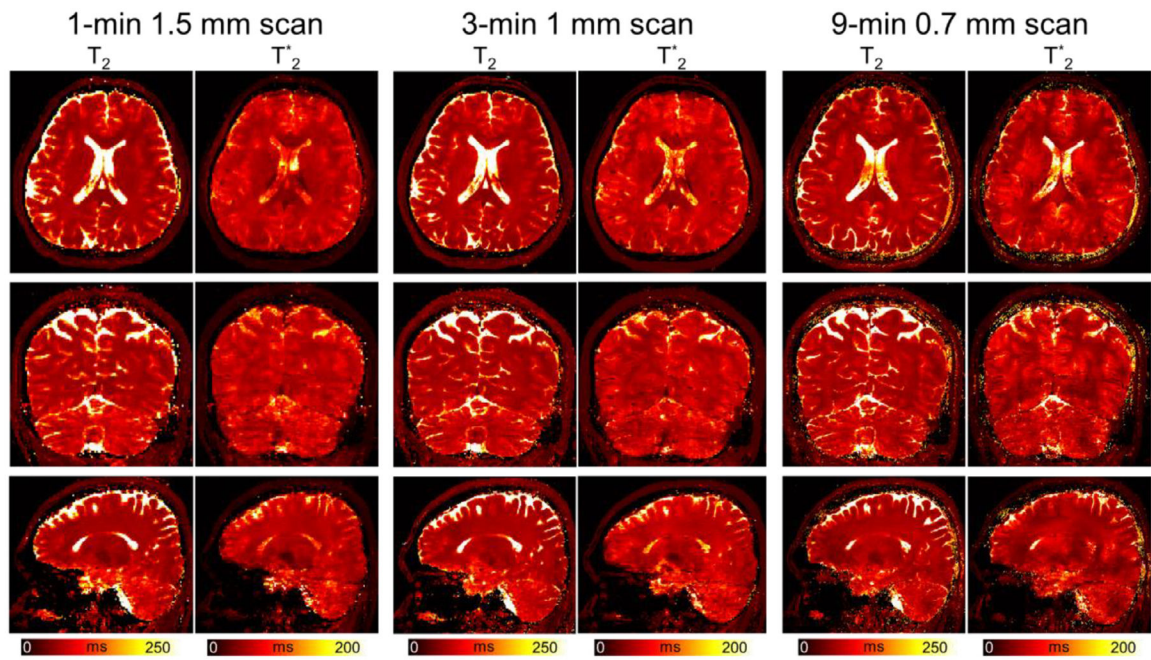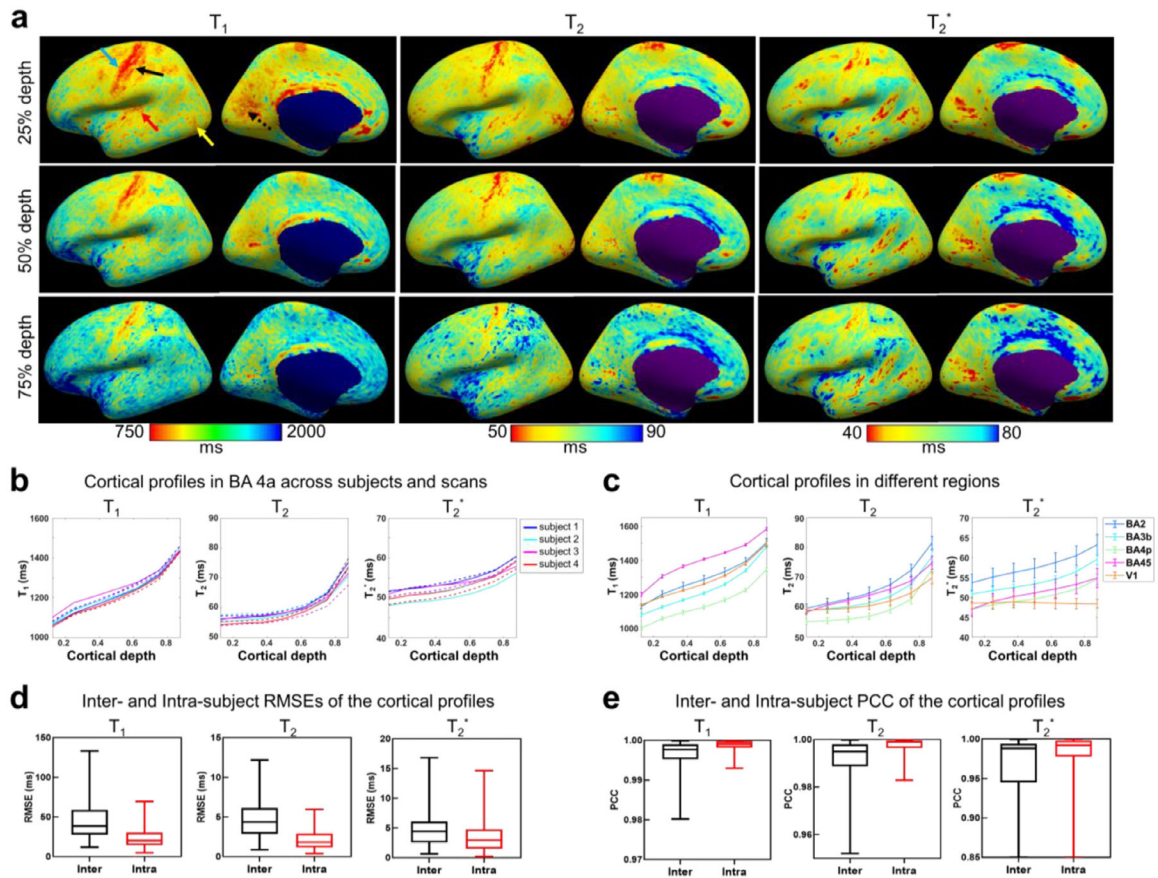
Fig. 7.
The estimated T_2 and T_2* maps from three different protocols on the same subject. Left panel: 1-minute protocol at 1.5-mm isotropic resolution; middle panel: 3-minute protocol at 1-mm isotropic resolution; right panel: 9-minute protocol at 0.7-mm isotropic resolution.

Fig. 8.

Surface-based cortical analysis of T_1, T_2 and T_2^* obtained from the 3D-EPTI data at 0.7-mm isotropic resolution. **a**, Quantitative parameters sampled at three different cortical depths (25%, 50%, 75%) shown on the reconstructed cortical surface. Lower quantitative values were observed in highly-myelinated regions such as motor (blue arrow), somatosensory (black arrow), auditory (red arrow), middle temporal visual area (yellow arrow) and visual cortex (dotted black arrow). **b**, Examples of quantitative values as a function of cortical depth (fraction of the cortical thickness) in the BA 4a area of the 4 subjects in the 2 repeated scans (solid line: scan 1, dashed line: scan 2). **c**, Averaged quantitative values over the 2 scans across 4 subjects as a function of cortical depth (fraction of the cortical thickness) in 5 representative ROIs. Error bars represent the standard deviations between the 4 subjects. **d**, Box plots of the root-mean-square-errors (RMSEs) of the cortical profiles between (inter) and within (intra) subjects. **e**, Box plots of the Pearson's correlation coefficients (PCCs) of the profiles between (inter) and within (intra) subjects.
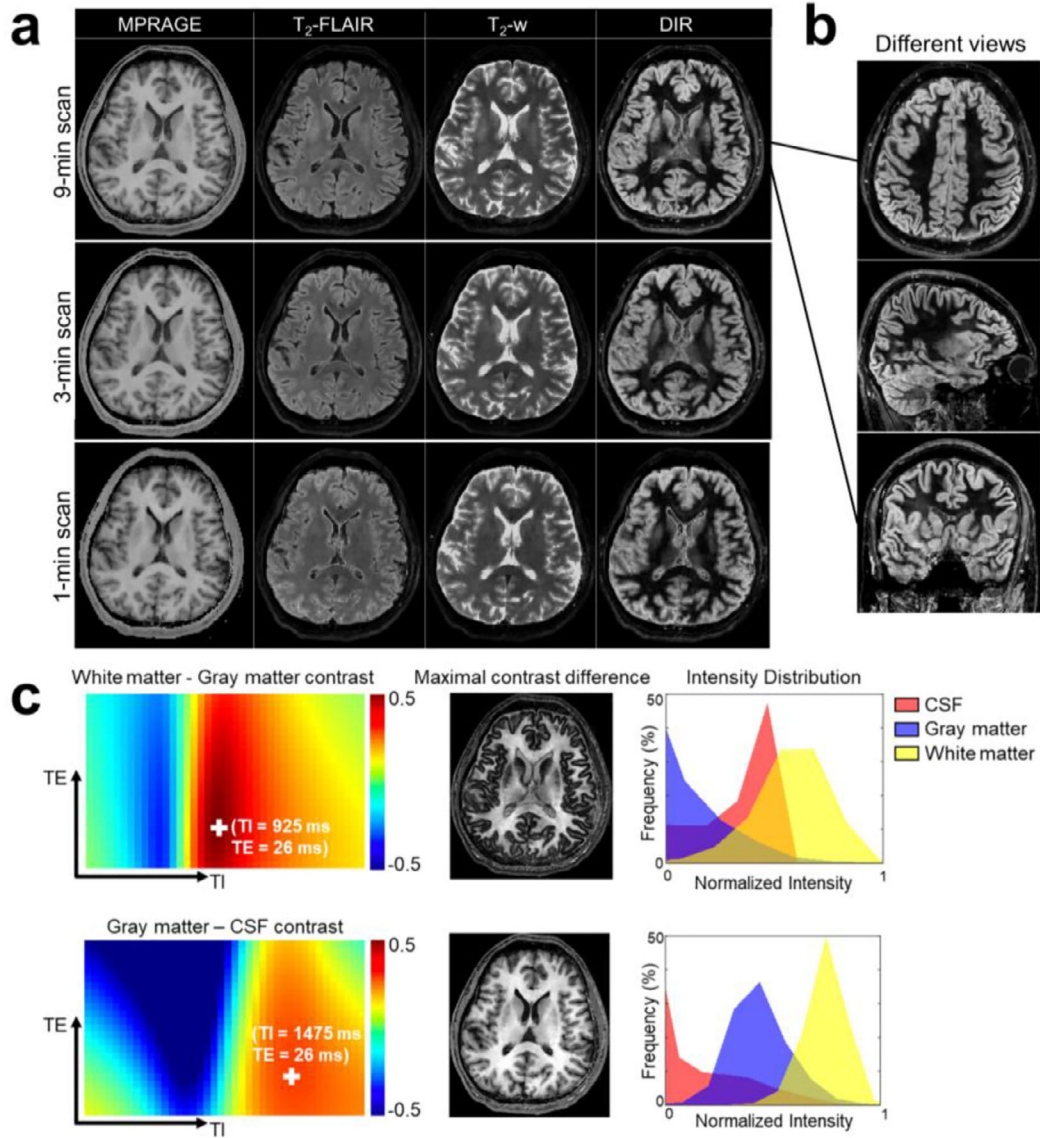
Fig. 9.
Synthesized multi-contrast images using 3D-EPTI. **a**, Synthetic MRRAGE, T_2-FLAIR, T_2-weighted, and double-inversion recovery (DIR) contrasts from the three protocols (9-min at 0.7-mm, 3-min at 1-mm, and 1-min at 1.5-mm). **b**, Different views of the synthesized DIR image at high resolution. **c**, left) Spectrum of contrast difference between the two tissues; middle) Images with maximal contrast difference between white and gray matter, and between gray matter and CSF; right) Intensity distribution in the three tissues.